Journal of Alloys and Compounds, 869(2021), 159232.

Anisotropic thermal lattice expansion and crystallographic structure of strontium aluminide within Al-10Sr alloy as measured by in-situ neutron diffraction

--Manuscript Draft--

Manuscript Number:	JALCOM-D-20-00434R1
Article Type:	Full Length Article
Keywords:	Intermetallics; Thermal expansion; Microstructure; thermal analysis; crystal structure; neutron diffraction
Corresponding Author:	Klaus-Dieter Liss, Dr. rer. nat. Technion - Israel Institute of Technology Shantou, CHINA
First Author:	Klaus-Dieter Liss, Dr. rer. nat.
Order of Authors:	Klaus-Dieter Liss, Dr. rer. nat.
	Stefanus Harjo
	Takuro Kawasaki
	Kazuya Aizawa
	Pingguang Xu
Abstract:	The aluminium strontium master alloy Al-10Sr has been investigated by in-situ neutron diffraction upon a heating-cooling cycle, revealing composition, crystallographic structure, lattice evolution and linear thermal expansion coefficients. Expansion of the Al matrix between [23.5 … 26.7]·10-6K-1 depends on temperature and fits well to the literature values, extrapolating to higher temperature at 800 K. Thermal expansion is highly anisotropic for tetragonal Al4Sr by a factor of 1.86 with values of 20.8 and 11.1 ·10-6K-1 in a and c-axis. The even larger discrepancy to the Al matrix is prone to residual intergranular phase stresses explaining the brittleness of such composite material. Upon first heating, recovery of the initially plastically deformed material is observed until 600 K and 700 K, for Al4Sr and Al. Rietveld analysis refines the 4e Wyckoff positions of the I 4/m m m crystal structure to z = 0.39 revealing that local tetrahedrons are regular while local hexagons are stretched, in contrast to literature. Its lattice parameters report to aI = 4.44240(48) Å, cI = 11.0836(15) Å at 300 K. Furthermore, the manuscript demonstrates full technical analysis of the neutron data. Findings feed into data bases and an outlook for improving mechanical properties of Al4Sr composites is given.
Order of Authors (with Contributor Roles):	Klaus-Dieter Liss, Dr. rer. nat.
	Stefanus Harjo
	Takuro Kawasaki
	Kazuya Aizawa
	Pingguang Xu

Journal of Alloys and Compounds, 869(2021), 159232.

Anisotropic thermal lattice expansion and crystallographic structure of strontium aluminide within Al-10Sr alloy as measured by in-situ neutron diffraction

Klaus-Dieter Liss[1,2,3,*], Stefanus Harjo[4], Takuro Kawasaki[4], Kazuya Aizawa[4], Pingguang Xu[5]

[1]Materials and Engineering Science Program, Guangdong Technion – Israel Institute of Technology, 241 Daxue Lu, Jinping Qu, Shantou, Guangdong 515063, China.

[2] Technion – Israel Institute of Technology, Haifa 32000, Israel.

[3] Faculty of Engineering & Information Sciences, University of Wollongong, Northfields Avenue, Wollongong, NSW 2522, Australia.

[4] J-PARC Center, Japan Atomic Energy Agency, Tokai, Ibaraki 319-1195, Japan.

[5] Materials Sciences Research Center, Japan Atomic Energy Agency, Tokai, Ibaraki 319-1195, Japan.

* corresponding author: kdl@gtiit.edu.cn; kdliss@technion.ac.il; liss@kdliss.de

Keywords: intermetallics; thermal expansion; microstructure; thermal analysis; crystal structure; neutron diffraction;

Abstract

The aluminium strontium master alloy Al-10Sr has been investigated by in-situ neutron diffraction upon a heating-cooling cycle, revealing composition, crystallographic structure, lattice evolution and linear thermal expansion coefficients. Expansion of the Al matrix between $[23.5 \ldots 26.7]\cdot 10^{-6}K^{-1}$ depends on temperature and fits well to the literature values, extrapolating to higher temperature at 800 K. Thermal expansion is highly anisotropic for tetragonal Al_4Sr by a factor of 1.86 with values of 20.8 and 11.1 $\cdot 10^{-6}K^{-1}$ in *a* and *c*-axis. The even larger discrepancy to the Al matrix is prone to residual intergranular phase stresses explaining the brittleness of such composite material. Upon first heating, recovery of the initially plastically deformed material is observed until 600 K and 700 K, for Al_4Sr and Al. Rietveld analysis refines the *4e* Wyckoff positions of the `I 4/m m m` crystal structure to $z = 0.39$ revealing that local tetrahedrons are regular while local hexagons are stretched, in contrast to literature. Its lattice parameters report to $a_I = 4.44240(48)$ Å, $c_I = 11.0836(15)$ Å at 300 K. Furthermore, the manuscript demonstrates full technical analysis of the neutron data. Findings feed into data bases and an outlook for improving mechanical properties of Al_4Sr composites is given.

Graphical Abstract:

Photograph of the dilatometer furnace for in-situ neutron scattering at the Takumi beamline, J-PARC, Japan, superimposed by insights into a Williamson-Hall plot (left) and crystal structure of Al_4Sr (right).

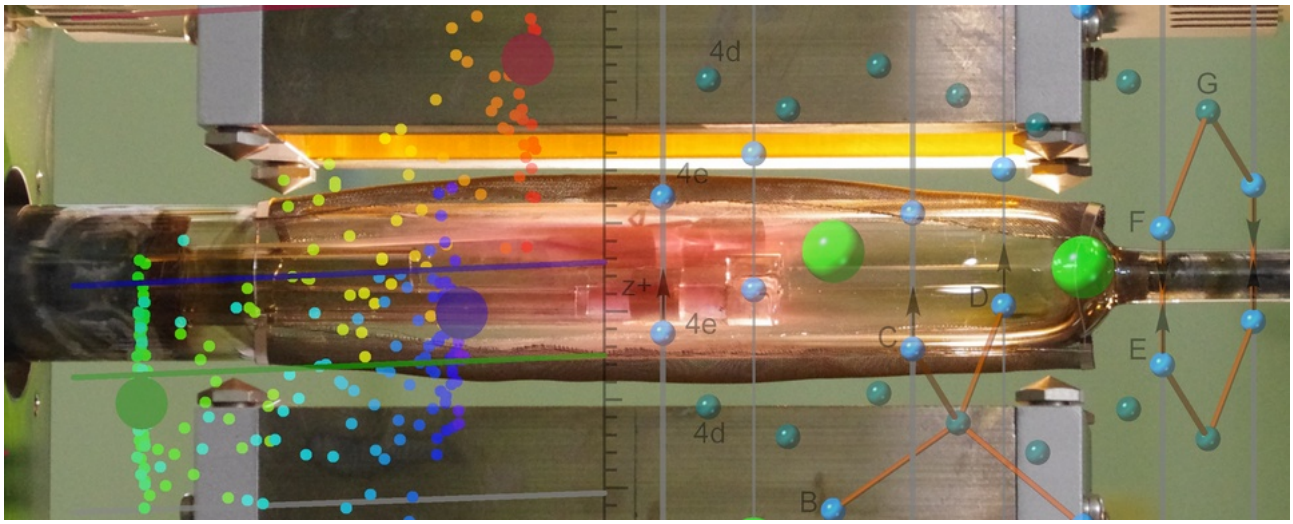

1. Introduction

Although strontium intermetallics play a huge role as precipitates in composite aluminium and magnesium alloys, nothing is known on their crystallographic thermal expansion, which is an important parameter for modeling and optimizing thermo-mechanical processing and the final mechanical properties of such material. Strontium aluminide in particular, is largely used as grain refiner inhibiting dendritic grain growth in casting processes of both aluminium and magnesium alloys [1],[2],[3]. It largely delays the nucleation and growth kinetics of intermetallics in cooling melt and suppresses inhomogeneities by gravitational setting [4]. Moreover, a whole range of metal matrix composites are in focus of research for strengthening light-weight alloys upon further processing and heat treatment. Frerichs states in 2011 in his thesis [5] that several deformation processed metal matrix composites with an Al matrix have been reported, including Al-Ti, Al-Sn, Al-Mg, and Al-Nb but nothing was found on Sr-Al matrix compounds, though elongated heat treatments at higher temperature of deformation-processed composites may precipitate Al-Sr intermetallics. Because of an assumed high-stiffness of the intermetallics, investigations are undertaken in Sr-Al deformation-processed metal matrix composites to serve as wires for high-voltage cables with good mechanical and electrical properties. In another thesis in 2012, Gorny concludes upon the formation and characterization of major intermetallic phases in Al-xSi-yFe-zSr alloys that physical properties and beyond them, their thermal expansion behavior are typical research topics that would yet have to be explored [6]. Meanwhile, Ashrafi et alii reported in 2015 [7] that hardness increases with adding Al-10Sr to the melt, while the ultimate tensile strength does not increase or only little. The weak interface between the particles and the matrix was made responsible to decrease this strength. A hardness maximum was found at 0.5 % mass of Al-10Sr to the melt. Allover, the material shows high stiffness and strength but low resistance to fracture. Those trends are seconded in a further investigation by Biswas et alii [8] stating brittleness increases with Al_4Sr fraction in Al-5Mg-$x$$Al_4Sr$ compounds ($x \in 0...7.5$; mass-%). Maximum ductility reports to $x = 5$ % while a mixed fracture mechanism of both ductile and brittle evolves at increasing concentrations. Crack initiation is made responsible on the interfacial properties between the matrix and Al-10Sr phases.

The lack of knowledge of fundamental thermal lattice expansion of Al_4Sr motivates the present work, which is found to be very distinct from the matrix and therefore needs to be considered for the evolution of intergranular stresses contributing to such as interface adhesion, tensile and fracture behavior. In-situ neutron diffraction has been chosen to follow the signal upon a heating-cooling cycle, which is evaluated in detail to determine lattice expansion for both the Al matrix and Al_4Sr intermetallics and to refine their crystallographic parameters.

2. Crystallography

Strontium aluminide, Al_4Sr crystallizes in the tetragonal barium aluminide structure Al_4Ba with Hermann Mauguin notation I 4/m m m, international space group number 139 and Strukturbericht designation $D1_3$. Pearson describes the Wyckoff positions [9] of such isomorphs with Sr on the 2(a) positions at cell coordinates [0 0 0], Al(1) on 4(d) and Al(2) with [0 ½ ¼] on 4(e) with [0 0 *z*]. Lattice parameters of *a* = 4.459 Å and c = 11.07 Å have been reported by Nowotny & Wesenberg in 1939 [10] [11] after conversion of kX units to Å (by 1.00202, see [12] – note, some literature, including the ICSD database entry 107887 (2008) mistakenly omit this factor) and *z* = 0.38. Aluminum is well known to crystallize *fcc* close-packed in space group F m $\bar{3}$ m, number 225, Strukturbericht A1, and lattice parameter of *a* = 4.04961 Å [13], COD entry 9012002. Note, the Crystallographic Open Database, COD has reviewed and corrected all omitted kX value conversions based on Straumanis [13] entries upon discrepant measurements by the present study. The Al-Sr phase diagram has been published by Bruzzone and Merlo in 1975 [14] revealing that both Al and Al_4Sr form line compounds which are insolvable to each other. Even recent literature on the Al-Mg-Sr phase diagram [15] only consider insolubility between these two compounds. Information on point defects is lacking, which could be helpful to determine lattice parameter variations. According to reviewed data in Landolt-Börnstein [16] the composition starts melting in a eutectic reaction at about 933 K.

Regarding the lattice parameters and crystal structures of both phases, there exist no similar atomic distances or planes which may form a coherent interface. No report on orientation correlations can be found. Moreover, the intermetallic forms in needle or rod shape habitus when precipitating from the melt and phase boundaries may show irregular and curved manifolds when the Al_4Sr fraction is high [17] [8]. All these are indications of incoherent phase boundaries.

3. Experimental

A heating-cooling cycle has been undertaken on a cuboid shaped Al-10Sr specimen after height reduction from 12.1 mm to 8.25 mm by hammering. This plastic strain of ε = -32 % was intended to break potential large grains into more favorable mosaic structure, suitable for neutron diffraction. We have used the engineering neutron diffractometer Takumi (匠) [18] within the Materials and Life Science Experimental Facility [19], [20] at the J-PARC neutron spallation source [21] in Japan. A halogen-lamp heated dilatometer furnace has been mounted into the sample position under an incident angle of 45° and scattering angle of ± 90° in order to probe for scattering vectors both longitudinal and transverse to the specimen compression axis. Time-of-flight histograms of 30 s

acquisition bins have been established from the event-mode data and calibrated to scattering vector transfer units Q by $Q = 15000 \cdot 2\pi/\tau$, where τ is the instrument-corrected and calibrated neutron time of flight. Note, for Rietveld analysis and absolute lattice parameter determination, the factor 15000 has been refined to an instrument function, however, for relative shifts as in $\Delta Q/Q$ we work with the given value for single-peak-fitting, as it does not fall into account. Peak widths and integrated peak intensities are then transformed by $\Delta Q/Q = -\Delta\tau/\tau$ and $I_Q/Q = I_\tau/\tau$, respectively. Similarly, peak shifts ΔG of a given reflection G are evaluated by the lattice strain $\varepsilon = -\Delta G/G = \Delta\tau/\tau$. Intensity channels have been normalized point by point by a smooth function – a 16th order polynomial fit to recordings of an isotropic vanadium scatterer, see Figure (1). An overall normalization for each time slice has been undertaken by the actual proton current of the spallation source [21]. All normalization procedures have been scaled to some determined nominal value to operate with factors close to 1, in order to mostly preserve the counting statistics. For each 30 s time step, peak positions have been evaluated by individual peak fitting of Gaussians using the *Igor Pro 4* software and the *Multi-Peak-Fitting* package. A Rietveld analysis using the *Maud* program has been applied to the summed data during the holding time at 800 K. Figure (2) shows the diffractograms color coded against scattering vector and time, together with the internally calibrated temperature, see below. The Takumi data set identification is 5354 and run number ENG022688.

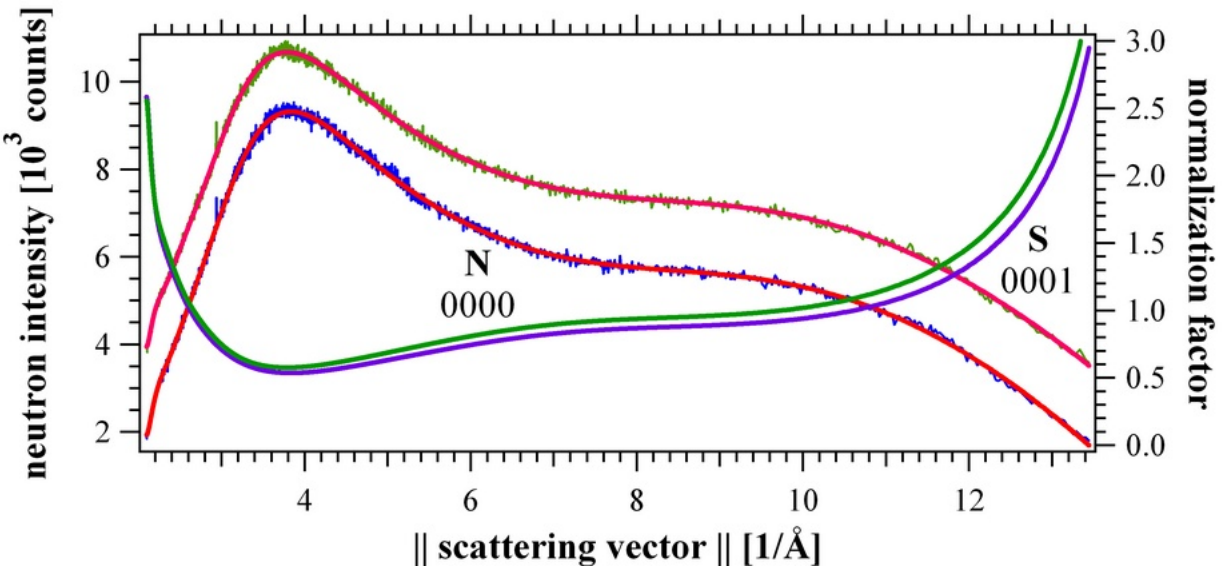

Figure 1: Intensity calibration by fitting polynomials to the statistics-prone vanadium scattering (top lines in the middle) and evaluated smooth channel-by-channel multiplication factors close to 1 (bottom lines) for both north (N, 0000) and south (S, 0001) detector banks [18] [19]. (data set ENG022249)

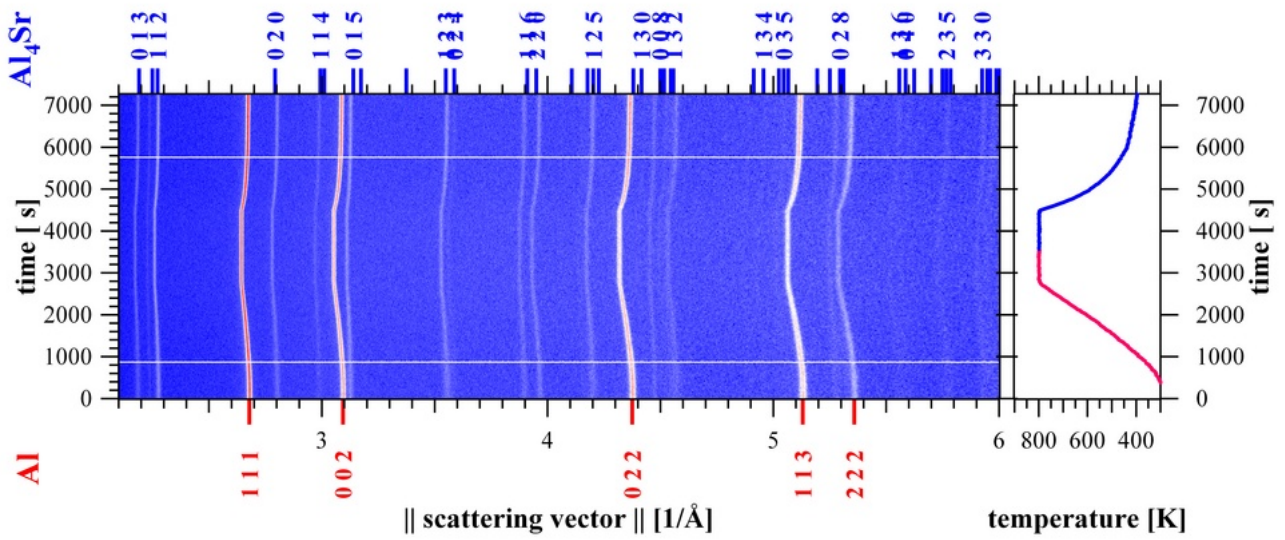

Figure 2: Neutron diffractograms recorded as a function of time (left) while temperature was varied (right). Blue: low intensity; white: medium intensity, red: high intensity. Two phases are abundant and reflections are indexed

4. Temperature profile and internal calibration

The applied temperature cycle is shown to the right in Figure (2). It was intended to heat from room temperature to 800 K with 0.25 K/s, hold for 1800 s and cool by -0.5 K/s. However, it turns out that the thermocouple readings do not represent the lattice response of the specimen. Because of an experimental lag and time-dependent offset to the thermo-couple reading, we calibrate the sample temperature at each time step through the measured lattice strain ε and second-order thermal expansion of the Al matrix, together with the measured holding points at T_{min} = 294.1 K and T_{max} = 799.9 K with strain values ε_{min} and ε_{max}, respectively – i.e. when the thermocouple had time to equilibrate with the sample. With $T_{min} \approx T_R$ close to room temperature T_R we derive

$$\varepsilon_{max} - \varepsilon_{min} = \Delta\varepsilon = \eta\,\Delta T = (\eta_0 + \zeta T)(T - T_R) \quad , \tag{1}$$

which is a quadratic equation in temperature T. In order to solve $T(\varepsilon)$ we rewrite equation (1)

$$\alpha T^2 + \beta T + \gamma = 0 \quad \text{and solution} \quad T = \frac{-\beta + \sqrt{\beta^2 - 4\alpha\gamma}}{2\alpha} \tag{2}$$

with

$$\alpha = \zeta\,;\ \beta = \eta_0 - \zeta T_R\,;\ \gamma = -(\Delta\varepsilon + \eta_0 T_R) \tag{3}$$

With $\eta_0 = 20.94(13)\cdot10^{-6}$ K^{-1} and $\zeta = 7.37(23)\cdot10^{-9}$ K^{-2} we calibrate the temperature profile $T(\varepsilon)$ as shown to the right in Figure (2). Such quadratic regression of thermal expansion has been essential as it may lead up to 17 K temperature difference values as compared to linear terms only.

The temperature dependence of the linear thermal expansion coefficient $\eta = \eta_0 + \zeta T$ has been

regressed from literature published by Hidnert in 1924 [22] on pure aluminum, as displayed in Figure (3). The data point of the present study heating from T_{min} = 294.1 K and T_{max} = 799.9 K fits excellently its extrapolation and now confirms the behavior until 800 K.

Such excellent agreement validates the usage on internal temperature calibration by the lattice expansion of the Al matrix. Moreover, as Sr does not dissolve at all in Al, lattice parameter variations of the latter due to chemical concentration changes, as in titanium aluminides [23] and zirconium niobium alloys [24] can be disregarded.

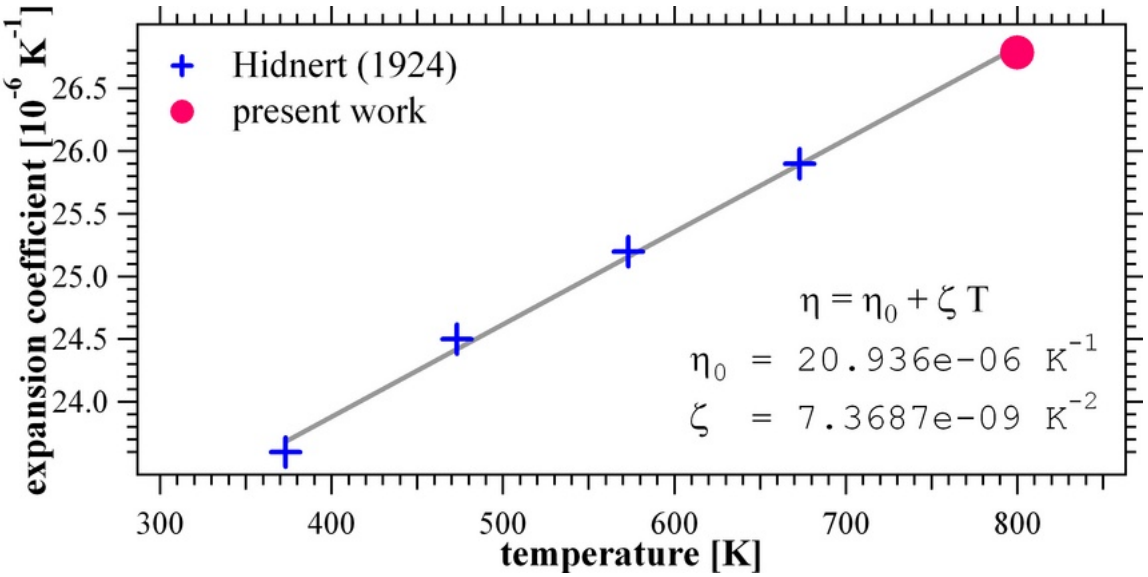

Figure (3): Variation of linear thermal expansion coefficient η of aluminum as per Hidnert (Table 4 in [22], blue crosses) and the present work (red marker).

5. Rietveld Refinement

Figure (4) displays a simple Rietveld refinement at the holding temperature 800 K, allowing an integrated acquisition time of 1600 s. The mass fraction of Al_4Sr results in 13.6 %, balanced by *fcc* Al. This leads to an overall mass composition of Al-6.1Sr, lying lower than the nominal composition of Al-10Sr, which should have revealed 22.3 % of Al_4Sr. Comparison of the two orthogonal scattering directions at Takumi yields some fluctuations in the individual peak heights which must be related to grain orientation effects, see for example Xu et alii [25]. This discrepancy in composition is not followed further in this work, as there is not much phase evolution; more interestingly we focus on the change of the lattice parameters. The latter have been refined to a_{Al} = 4.08683(37) Å for aluminum and a_I = 4.48908(48) Å, c_I = 11.2064(15) Å for Al_4Sr at 800 K.

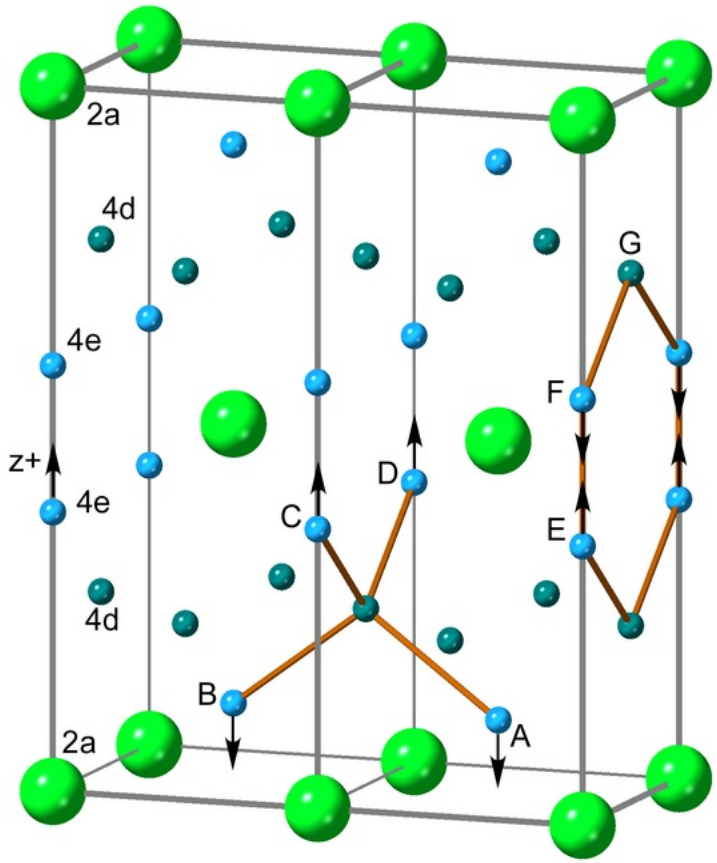

Figure (5): Sketch of two Al_4Sr unit cells, emphasizing configurations of aluminum hexagons and tetrahedrons. Sr(1) positions on 2a: large, green; Al(1) positions on 4d, small, gray blue; Al(2) positions on 4e: small, light blue. The arrows indicate increasing *z* coordinate. Atoms A,B,C,D span a tetrahedron while E,F,G indicate two sides of a hexagon.

We further refined the position *z* of the Al(2) atoms, rendering $z = 0.3957$. Figure (5) displays a pair of unit cells indicating the locations of Al hexagons on the {100) faces as well as tetrahedral arrangements between the Al(1) and Al(2) atoms. According to Pearson, the tetrahedrons are *somewhat squashed in the [001] direction* [9]. Assuming a regular hexagon forming on the {100) faces would require $\overline{FE} = \overline{FG}$ and thus $z_{hex} = \frac{7}{12} - \sqrt{\frac{a^2}{12\,c^2} + \frac{1}{36}}$ evaluating $z_{hex} = 0.380$. This holds for pretty much all published *a* and *c* values (including our measured *a* and *c*) and indeed matches their values $z_{lit} = 0.38$. In other words, all literature describes the hexagons as regular, while the tetrahedrons are squashed along the [001] axis. In contrast, our results with $z = 0.3957$ elongate the hexagons significantly by 4 % in the [001] direction. Making the tetrahedron regular means $\overline{AB} = \overline{AC}$ leading to $z_{tet} = \frac{1}{4} + \frac{1}{\sqrt{(8)}}\frac{a}{c}$ computing with our measured lattice parameters

to $z_{tet} = 0.3916$. This matches very well our refined $z = 0.3957$, stating that the tetrahedral structures tend to attain ideal regular shape in cost of stretching the hexagons – opposite than assumed so far in literature.

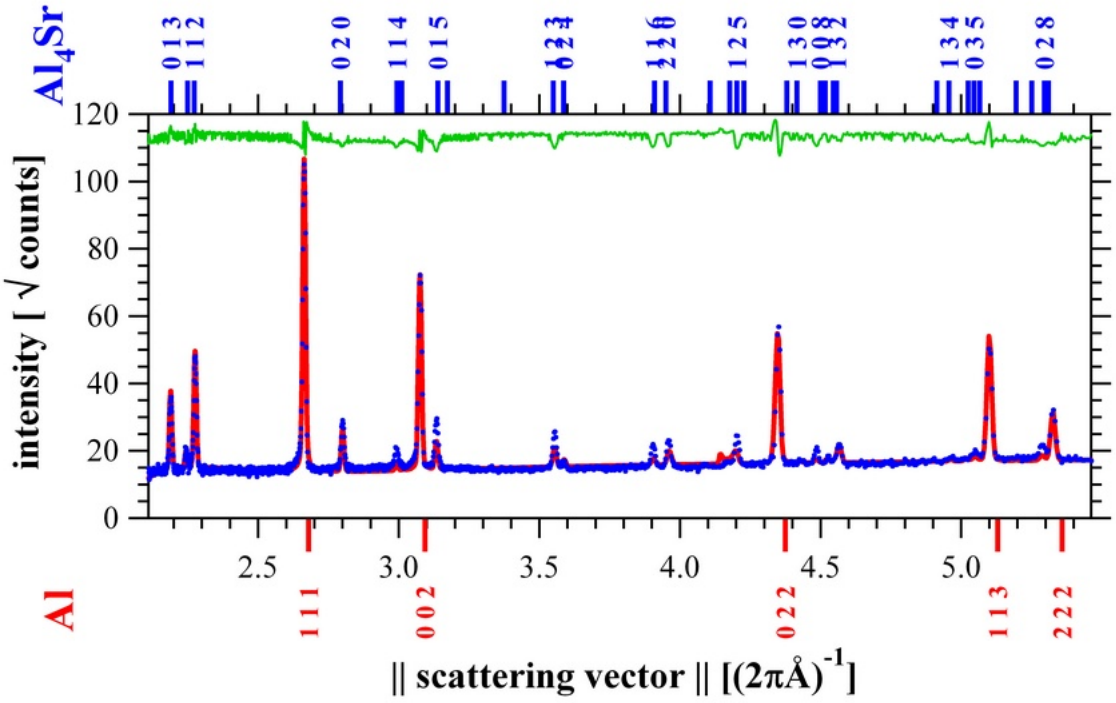

Figure (4): Rietveld refinement at holding temperature 800 K. Measured diffractogram in dots (blue), calculated in continuous line (red), and difference top (green, arbitrary units).

6. Aluminum peak broadening

Peak widths ΔG at full width half maximum are evaluated in Figure (6) by a Williamson-Hall analysis [26], at which a coherent crystallite size scales by the Scherrer formula with $2\pi/D$ into reciprocal space, often accompanied by a shape factor K for non plane-parallel particle habitus [27]. Thus, together with a gradient crystal part [28] of total strain amplitude ε and an instrument resolution function ΔQ_r it yields

$$\Delta G = (2\pi/D)\cdot K + \varepsilon G + \Delta Q_r \quad . \qquad (4)$$

Figure (6a) shows the data of all five aluminum peaks together with resolution measurements by LaB_6 , given by the smaller markers. Figure (6b) zooms into the locations around the Al-002 and Al-022 reflections. All peaks fit straight lines $\Delta Q = a + b\ Q$, the Williamson-Hall equation with common axis offset a and individual slopes b_j . Data is shown for the entire heating-holding-cooling cycle, while three locally time-averaged values are extracted at initial state (*i*), holding at 800 K (*h*) and final state (*f*). Note, the displacements on the abscissa are due to thermal expansion. The

resolution function scales with $\Delta Q_r = b_r\, Q$. Assuming Lorentzian reflection profiles, we subtract the resolution broadening from the aluminium peak widths, resulting in a negligible grain size term, or physically meaning, in grain sizes of the micrometer and above range. The initial, holding and final total strain amplitudes $\varepsilon_{i,h,f} = b_{i,h,f} - b_r$ result in $\varepsilon_i = 1.30 \cdot 10^{-3}$, $\varepsilon_h = 0.36 \cdot 10^{-3}$ and $\varepsilon_f = 0.60 \cdot 10^{-3}$. The relative peak width evolution as a function of time, displayed in Figure (7), showing an initial decrease which is strict linear to temperature, disemboguing into a constant value at about 700 K onwards. The initial decrease is due to the annealing of distorted crystal lattice due to the uniaxial compression processing prior to the experiment. Upon cooling, there is very minor increase of the peak width.

In the concluding scenario, strain broadening decreases due to recovery upon heating from $\varepsilon_i = 1.30 \cdot 10^{-3}$ to a minimal value of $\varepsilon_h = 0.36 \cdot 10^{-3}$ above 700 K and holding at 800 K. Upon cooling, the system becomes stiff and eventually mismatching thermal expansion coefficients between the Al matrix and Al_4Sr leads to a slight increase of stress-induced strain to $\varepsilon_f = 0.60 \cdot 10^{-3}$.

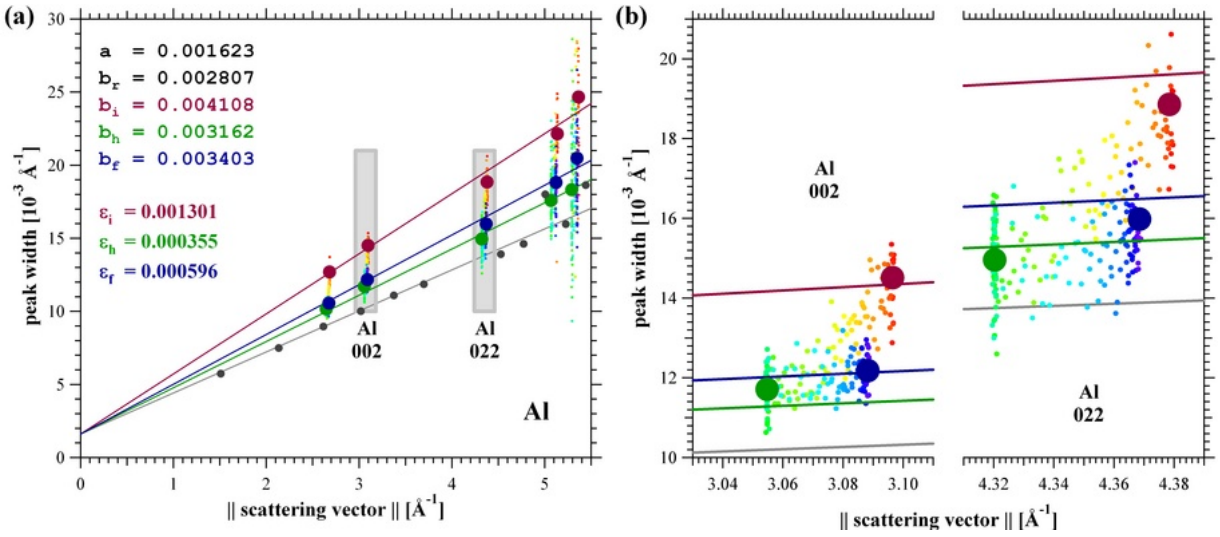

Figure (6): Williamson-Hall evaluation of peak broadening from aluminum. Figure (6b) zooms into the outlined areas in (a). The red, green and blue markers represent the average data at initial (i), holding (h) and final (f) condition, while the smaller dark markers represent LaB_6 data for obtaining the resolution function (r). Solid lines are linear fits $\Delta Q = a + b\, Q$ with common offset a. Microstrain $\varepsilon_{i,h,f} = b_{i,h,f} - b_r$. The dots are data taken at each timestep gradually changing color from red to green and blue upon heating holding and cooling.

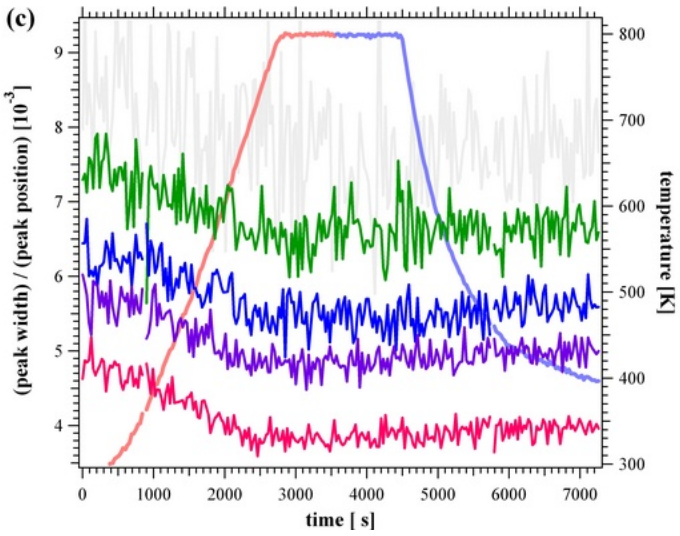

Figure (7): Peak widths at half maximum divided by peak position for the aluminum reflections 111, 002, 022, 113, 222 with ordinate offsets of $[0, 1, 2, 3, 4]\cdot 10^{-3}$), respectively, underlaid by the temperature profile.

7. Thermal expansion of Al_4Sr

Thermal evolution of lattice strain in Al_4Sr has been evaluated for the 8 reflections *hkl* as listed in Table 1 and displayed in Figure (8). The overall lattice expansion shows a clear difference between heating and cooling, expressed by a smaller and larger strain amplitude, respectively. Upon cooling, the behavior is strictly linear with slope η_c, while the heating curve starts initially with a smaller slope η_h until about 600 K and then following also η_c. This transition temperature coincides closely with the disappearance of intergranular strain broadening in Al, see Figure (7). The slopes at high temperature and cooling reveal the linear thermal expansion coefficients η_G, respectively in their crystallographic orientation $\hat{G}$, where their orientation angles Ψ towards the *c* axis are compiled in Table 1. The $\sin^2(\Psi)$ plot in Figure (9b) fits very well to a straight line, indicating an anisotropy ellipse which is maximal allowed under the crystal symmetry, and the refined values are $\eta_a = 20.8(2)\cdot 10^{-6}\,K^{-1}$ and $\eta_c = 11.1(2)\cdot 10^{-6}\,K^{-1}$ with a ratio of 1.86 . In a similar way, the initially smaller expansion on heating evaluates to $\eta_a^i = 14.0(8)\cdot 10^{-6}\,K^{-1}$, $\eta_c^i = 6.9(8)\cdot 10^{-6}\,K^{-1}$ and ratio 2.01, see Figure (9a).

G [Å^{-1}]	*h k l*	η_h [$10^{-6}\,K^{-1}$]	η_c [$10^{-6}\,K^{-1}$]	Ψ [°]	$\sin^2(\Psi)$
2.24	0 0 4	7.2	10.9	0.0	0.00

3.13	0 1 5	7.3	13.2	26.5	0.20
2.19	0 1 3	9.2	15.4	39.8	0.41
2.99	1 1 4	11.0	15.1	41.4	0.44
4.20	1 2 5	11.2	16.8	48.1	0.55
2.27	1 1 2	12.5	18.3	60.5	0.76
3.55	1 2 3	13.4	18.6	61.7	0.78
2.80	0 2 0	13.0	20.8	90.0	1.00

Table (1): List of scattering vectors with modulus G, Miller indices hkl, linear expansion coefficients η_h and η_c upon heating and cooling, respectively, orientation angle Ψ towards the c-axis, and its $\sin^2(\Psi)$.

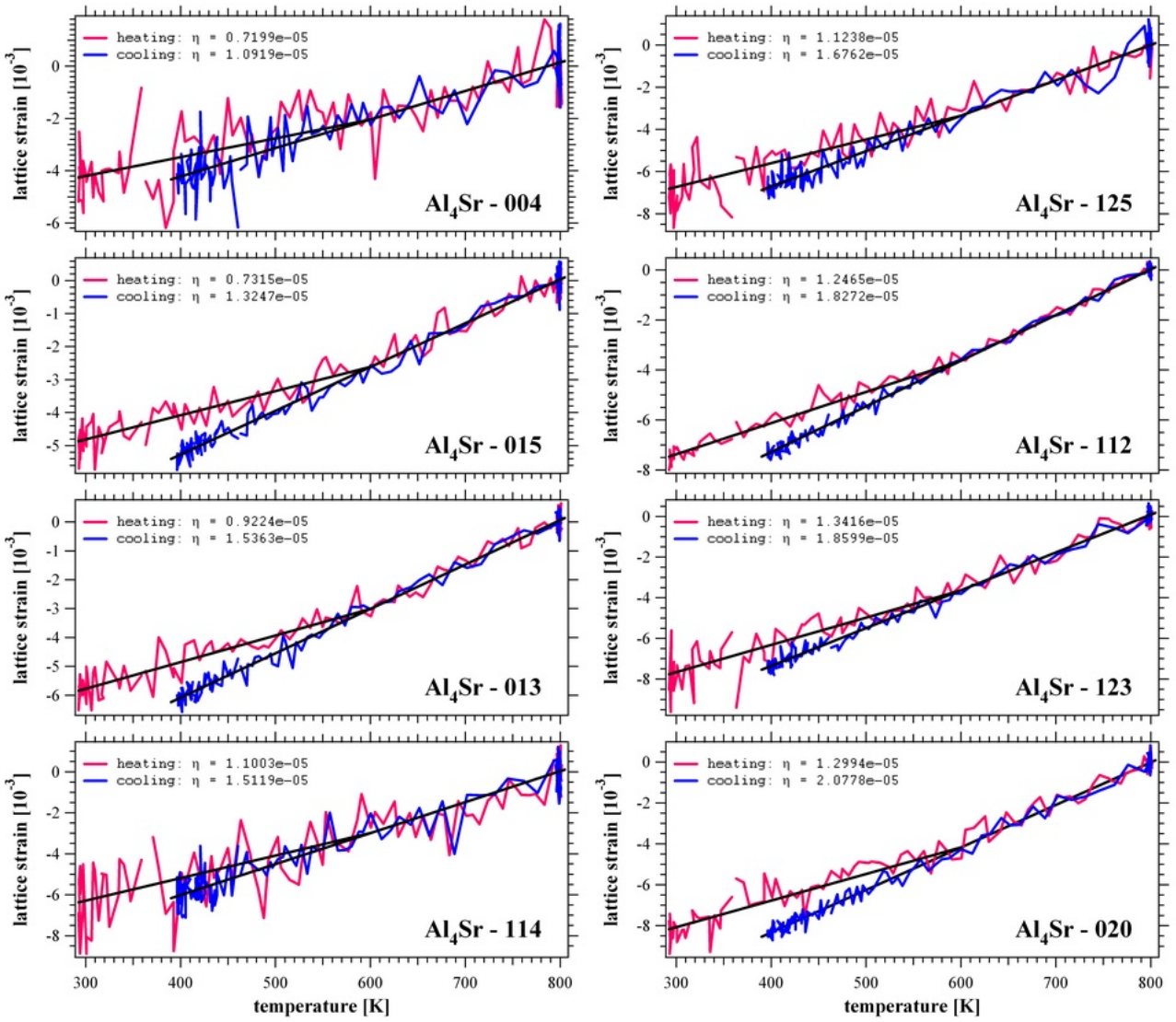

Figure (8): Thermal lattice strain in Al_4Sr measured on various reflections. The continuous lines are linear fits in the recovery range upon heating to 600 K and upon pure thermal expansion above 600 K, coinciding with cooling. The slope η is the linear thermal expansion coefficient for the given reflection.

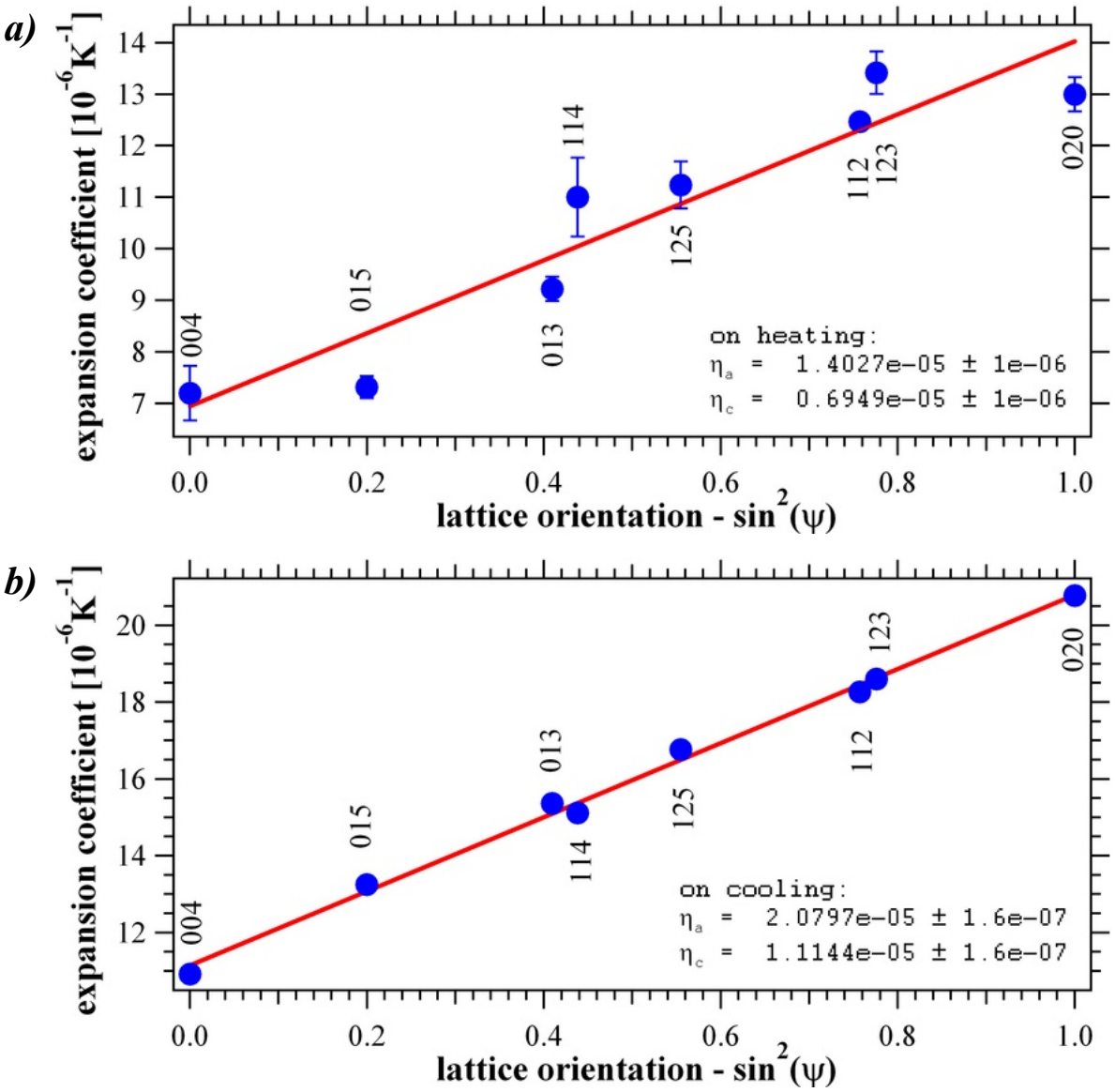

Figure (9): Thermal expansion coefficient versus lattice orientation in $\sin^2(\Psi)$. Fig. (a) shows results upon heating where lattice recovery plays a role on the expansion, while (b) as obtained on cooling follows linear thermal expansion.

8. Discussion

A series of lattice effects are occurring during in-situ heating of the Al-10Sr alloy, which is composed of two phases, *fcc* Al and tetragonal Al_4Sr. Their measured mass abundances are 86.4 % and 13.6 %, which renders a little lower than expected. The free parameter z of the Al_4Sr on the 4e Wyckoff positions (see Figure (5)) has been refined to $z = 0.3957$, showing that the Al tetrahedrons in the crystal structure are close to regular, while the hexagon configurations are somewhat stretched. This value does not change significantly with temperature. Upon heating, the plastically deformed material first recovers, expressed by both change of peak width and the value of linear

thermal expansion in Al_4Sr. Figure (9) reveals that expansion is lower upon heating and with larger scatter on the reflections, as it depends on non-eqiilibrium segregation, dislocations and stresses to the embedded matrix, which recover at 600 K, then following purely linear thermal lattice expansion.

For the Al phase, the peak widths decrease until 700 K due to a larger microstrain relaxation stored in the deformed material, while upon cooling, only a tiny microstrain develops due to a thermal expansion mismatch between the phases, and a relatively long cooling time, see Figures (6) and (7). Linear thermal expansion of Al matches very well the second order behavior published by Hidnert et alii [22] and therefore has been used as an internal temperature standard, Figure-(3). The Al_4Sr expansion curves, however, show an increase in slope at 600 K upon heating, which is maintained upon cooling. Recovering lattice defects established by the preceding plastic deformation would not have such large effect on the average lattice parameter and volumetric strain, therefore we attribute the reduced thermal expansion at first heating to a change of stoichiometry – as it has been frequently observed in other alloy systems [23],[24]. Although Al_4Sr is a line compound in the binary phase diagram, out-of equilibrium compositions may exist in the as-received sample. Moreover, the presence of the eutectic reaction between Al and Al_4Sr demands for some out-of-stoichiometry composition, although small. Linear thermal expansion of Al_4Sr is anisotropic and the measured strain ellipsoid matches the crystal symmetry. Along the *a*-axis, linear thermal expansion is almost double the value than along the *c*-axis, with $\eta_a = 20.8(2)\cdot 10^{-6}\,K^{-1}$ and $\eta_c = 11.1(2)\cdot 10^{-6}\,K^{-1}$, respectively, and both values lie well below that for Al with $\eta_{Al} \in [23.5 \ldots 26.5]\cdot 10^{-6}\,K^{-1}$ depending on temperature. On a quench over 500 K, this difference in thermal expansion between the intermetallic and aluminum can amount up to $15\cdot 10^{-6}\,K^{-1}$ and is prone to build up intergranular stresses. Elastic constants for pure Al are c_{11} = 110 GPa, c_{44} = 31 GPa [29] and yield strengths are 10 MPa to 500 MPa, depending on the alloy and microstructure. Thus, a simple calculation can render stress amplitudes of 800 MPa longitudinal and 230 MPa in shear upon such 500 K quench. Some of such stresses would relax though various mechanisms, but evidently some will remain and bias the system close to their yield limits, which is the reason why the alloys with higher Sr concentration become very brittle. Moreover, the Al and Al_4Sr crystal structures do not expose common lattice planes, which enhances the brittleness at their interfaces. Laio et alii's observation [30] that the size of the precipitaties plays a significant role on the mechanical properties can be explained by our found mismatch in thermal expansion, as larger precipitates, thus longer interfaces would build up higher intergranular stresses which lead to failure. Crystal symmetry in such reported needle- or rod-shaped precipitates favors the *c*-axis along the rod axis, even exposing maximum mismatch of thermal expansion on the longer [001] zone interfaces, which is very

unfortunate. As the processing route for designing the microstucture and morphologies of precipitates is extremely important for the mechanical properties [30] it is suggested here to investigate plate shaped precipitates with their normal along *c*. Such configuration would minimize thermal expansion stresses along the [001] zone planes, while the {001} interfaces show only minor mismatch between their expansion coefficients η_a and η_{Al}. Together with our here reported results, new processing and cooling routes can be engineered.

9. Conclusions

The present study on Al-10Sr (mass.%) reports on various crystallographic, structural and microstructural properties and their evolution upon a heating and cooling cycle.

- Crystal structure: Opposite to literature, we find that the tetrahedral configurations of Al atoms are of ideal regular shape while the Al hexagons on the {100) faces are stretched. The corresponding Wyckoff position parameter is $z = 0.3957$.
- Rietveld refinement reveals 2 phases, *fcc* Al with 86.4 % and tetragonal Al_4Sr with 13.6 %.
- The linear thermal expansion of Al has a second order term and the presently reported value at 800 K matches excellently its extrapolation from literature.
- The Al matrix recovers linearly with temperature from the initially strongly deformed microstructure with microstrain $\varepsilon_i = 1.30 \cdot 10^{-3}$ and reaches an almost stress-free state at and above 700 K with $\varepsilon_h = 0.36 \cdot 10^{-3}$. Upon cooling, a slight microstrain builds up to $\varepsilon_f = 0.60 \cdot 10^{-3}$ due to inter-phase stresses driven by mismatching thermal expansion coefficients.
- As-received Al_4Sr is out of equilibrium stoichiometry and recovers upon first slow heating.
- Al_4Sr shows a strong anisotropy in linear thermal expansion by a factor of 1.86 between *a* and *c* direction. With values of $\eta_a = 20.8(2) \cdot 10^{-6}\,K^{-1}$ and $\eta_c = 11.1(2) \cdot 10^{-6}\,K^{-1}$, it is considerable smaller than that of Al with $\eta_{Al} \in [23.5 \ldots 26.7] \cdot 10^{-6}\,K^{-1}$.
- The mismatch of thermal expansion can build up thermal intergranular stresses which depend very much on the crystallographic interface. They bias external applied load and lead to increased brittleness.
- The often observed rod-like habitus is most unfavorable and plate-shaped precipitates would be better to reduce brittleness and enhance mechanical properties.
- The thermal expansion results are essential for modeling the material.
- Refined lattice parameters of Al_4Sr are $a_l = 4.48908(48)$ Å, $c_l = 11.2064(15)$ Å for Al_4Sr at 800 K. Together with the thermal expansion coefficient, the room-temperature values

calculate to a_I = 4.44240(48) Å, c_I = 11.0836(15) Å at 300 K.

Altogether, the here reported findings update the Crystallography Open Database [31] with entries 3000256 and 3000260 at 800 K and 300 K, respectively, and present first reports of thermal lattice expansion in Al_4Sr, which are important for modeling alloys of the Al-Sr system for fundamental and applied properties.

Acknowledgements

The authors like to thank the J-PARC facility for granting beam time under proposal number 2014A0267. KDL acknowledges The Bragg Institute, Australian Nuclear Science and Technology Organisation for travel and research support to perform this experiment. We appreciate Dr. Mark Reid to provide the specimen from University of Wollongong.

References

[1] D.G. Mallapur, S.A. Kori, K.R. Udupa, Influence of Ti, B and Sr on the microstructure and mechanical properties of A356 alloy, J. Mater. Sci. 46 (2011) 1622–1627. https://doi.org/10.1007/s10853-010-4977-3.

[2] M. Timpel, N. Wanderka, R. Schlesiger, T. Yamamoto, N. Lazarev, D. Isheim, G. Schmitz, S. Matsumura, J. Banhart, The role of strontium in modifying aluminium–silicon alloys, Acta Mater. 60 (2012) 3920–3928. https://doi.org/10.1016/j.actamat.2012.03.031.

[3] F.H. Froes, D. Eliezer, E. Aghion, The science, technology, and applications of magnesium, JOM. 50 (1998) 30–34. https://doi.org/10.1007/s11837-998-0411-6.

[4] S.G. Shabestari, M. Keshavarz, M.M. Hejazi, Effect of strontium on the kinetics of formation and segregation of intermetallic compounds in A380 aluminum alloy, J. Alloys Compd. 477 (2009) 892–899. https://doi.org/10.1016/j.jallcom.2008.11.037.

[5] A.E. Frerichs, Kinetics of Transformation in an In-situ Aluminum-strontium Deformation Processed Metal-metal Composite, Dissertation, Iowa State University, 2011. https://doi.org/10.31274/etd-180810-1741.

[6] A. Gorny, Characterization of Major Intermetallic Phases in solidified Al-xSi-yFe-zSr (x=2 to 12.5 wt%, y=0 to 0.5 wt% and z=0 and 0.02 wt%) alloys, Dissertation, McMaster University, 2012. http://hdl.handle.net/11375/12570.

[7] N. Ashrafi, A.H. Humod, Effect of Strontium and Silicon Carbide on Mechanical Properties of Aluminum Alloy (Lm 6), IOSR J. Mech. Civ. Eng. IOSR-JMCE. 12 (2015) 32–38.

[8] P. Biswas, A. Biswas, R. Bhandari, M.K. Mondal, Microstructure, mechanical properties and fracture behavior of in-situ Al-5Mg-Al4Sr composites, Mater. Today Commun. 15 (2018) 190–198. https://doi.org/https://doi.org/10.1016/j.mtcomm.2018.03.011.

[9] W.B. Pearson, The most populous of all crystal structure types—the tetragonal BaAl4 structure, J. Solid State Chem. 56 (1985) 278–287. https://doi.org/https://doi.org/10.1016/0022-4596(85)90177-X.

[10] H.N. Nowotny, H. Wesenberg, Untersuchungen im System Al-Sr, Z. Fuer Met. 31 (1939) 363–364.

[11] W.B. Pearson, A Handbook of Lattice Spacings and Structures of Metals and Alloys, Pergamon Press, 1958.

[12] W.L. Bragg, The conversion factor for kX units to \AAngström units, J. Sci. Instrum. 24 (1947) 27–27. https://doi.org/10.1088/0950-7671/24/1/105.

[13] M.E. Straumanis, The Precision Determination of Lattice Constants by the Powder and Rotating Crystal Methods and Applications, J. Appl. Phys. 20 (1949) 726–734. https://doi.org/10.1063/1.1698520.

[14] G. Bruzzone, F. Merlo, The strontium-aluminium and barium-aluminium systems, J. Common Met. 39 (1975) 1–6. https://doi.org/https://doi.org/10.1016/0022-5088(75)90212-X.

[15] D. Kevorkov, M. Medraj, M. Aljarrah, J. Li, E. Essadiqi, P. Chartrand, C. Fuerst, Experimental Study of the Al-Mg-Sr Phase Diagram at 400°C, J. Metall. (2014). https://doi.org/10.1155/2014/690623.

[16] B. Predel, Al-Sr (Aluminum - Strontium): Datasheet from Landolt-Börnstein - Group IV Physical Chemistry · Volume 12A: “Ac-Ag ... Au-Zr” in SpringerMaterials (https://dx.doi.org/10.1007/10793176_123), Springer-Verlag Berlin Heidelberg, n.d. https://doi.org/10.1007/10793176_123.

[17] M. Emamy, M. Oliayee, K. Tavighi, Microstructures and tensile properties of Al/2024–Al4Sr composite after hot extrusion and T6 heat treatment, Mater. Sci. Eng. A. 625 (2015) 303–310. https://doi.org/https://doi.org/10.1016/j.msea.2014.12.023.

[18] S. Harjo, T. Ito, K. Aizawa, H. Arima, J. Abe, A. Moriai, T. Iwahashi, T. Kamiyama, Current Status of Engineering Materials Diffractometer at J-PARC, Mater. Sci. Forum. (2011). https://doi.org/10.4028/www.scientific.net/MSF.681.443.

[19] K. Nakajima, Y. Kawakita, S. Itoh, J. Abe, K. Aizawa, H. Aoki, H. Endo, M. Fujita, K. Funakoshi, W. Gong, M. Harada, S. Harjo, T. Hattori, M. Hino, T. Honda, A. Hoshikawa, K. Ikeda, T. Ino, T. Ishigaki, Y. Ishikawa, H. Iwase, T. Kai, R. Kajimoto, T. Kamiyama, N. Kaneko, D. Kawana, S. Ohira-Kawamura, T. Kawasaki, A. Kimura, R. Kiyanagi, K. Kojima, K. Kusaka, S. Lee, S. Machida, T. Masuda, K. Mishima, K. Mitamura, M. Nakamura, S. Nakamura, A. Nakao, T. Oda, T. Ohhara, K. Ohishi, H. Ohshita, K. Oikawa, T. Otomo, A. Sano-Furukawa, K. Shibata, T. Shinohara, K. Soyama, J. Suzuki, K. Suzuya, A. Takahara, S. Takata, M. Takeda, Y. Toh, S. Torii, N. Torikai, N.L. Yamada, T. Yamada, D. Yamazaki, T. Yokoo, M. Yonemura, H. Yoshizawa, Materials and Life Science Experimental Facility (MLF) at the Japan Proton Accelerator Research Complex II: Neutron Scattering Instruments, Quantum Beam Sci. 1 (2017) 9. https://doi.org/10.3390/qubs1030009.
[20] K.-D. Liss, Materials and Life Science with Quantum Beams at the Japan Proton Accelerator Research Complex, Quantum Beam Sci. 2 (2018) 10. https://doi.org/10.3390/qubs2020010.
[21] H. Takada, K. Haga, M. Teshigawara, T. Aso, S.-I. Meigo, H. Kogawa, T. Naoe, T. Wakui, M. Ooi, M. Harada, M. Futakawa, Materials and Life Science Experimental Facility at the Japan Proton Accelerator Research Complex I: Pulsed Spallation Neutron Source, Quantum Beam Sci. 1 (2017) 8. https://doi.org/10.3390/qubs1020008.
[22] P. Hidnert, Thermal expansion of aluminum and various important aluminum alloys, Sci. Pap. Bur. Stand. 19 (1924) 697–731. https://doi.org/10.6028/nbsscipaper.179.
[23] X. Li, R. Dippenaar, J.-K. Han, M. Kawasaki, K.-D. Liss, Phase transformation and structure evolution of a Ti-45Al-7.5Nb alloy processed by high-pressure torsion, J. Alloys Compd. (2019). https://doi.org/10.1016/j.jallcom.2019.02.174.
[24] K. Yan, D.G. Carr, S. Kabra, M. Reid, A. Studer, R.P. Harrison, R. Dippenaar, K.-D. Liss, In Situ Characterization of Lattice Structure Evolution during Phase Transformation of Zr-2.5Nb, Adv. Eng. Mater. 13 (2011) 882–886. https://doi.org/10.1002/adem.201000350.
[25] P.G. Xu, Y. Tomota, Y. Arakaki, S. Harjo, H. Sueyoshi, Evaluation of austenite volume fraction in TRIP steel sheets using neutron diffraction, Mater. Charact. 127 (2017) 104–110. https://doi.org/10.1016/j.matchar.2017.02.028.
[26] G.K. Williamson, W.H. Hall, X-ray line broadening from filed aluminium and wolfram, Acta Metall. 1 (1953) 22–31. https://doi.org/https://doi.org/10.1016/0001-6160(53)90006-6.
[27] P. Scherrer, Bestimmung der Größe und der inneren Struktur von Kolloidteilchen mittels Röntgenstrahlen, Nachrichten Von Ges. Wiss. Zu Gött. Math.-Phys. Kl. (1918) 98–100.
[28] K.-D. Liß, Strukturelle Charakterisierung und Optimierung der Beugungseigenschaften von Si(1-x) Ge(x) Gradientenkristallen, die aus der Gasphase gezogen wurden, Doctoral Thesis, RWTH Aachen, 1994. http://darwin.bth.rwth-aachen.de/opus3/volltexte/2001/222/ (accessed October 27, 1994).
[29] J. Vallin, M. Mongy, K. Salama, O. Beckman, Elastic Constants of Aluminum, J. Appl. Phys. 35 (1964) 1825–1826. https://doi.org/10.1063/1.1713749.
[30] C. Liao, J. Chen, Y. Li, R. Tu, C. Pan, Morphologies of Al4Sr Intermetallic Phase and Its Modification Property upon A356 Alloys, J. Mater. Sci. Technol. 28 (2012) 524–530. https://doi.org/10.1016/S1005-0302(12)60092-9.
[31] S. Gražulis, A. Daškevič, A. Merkys, D. Chateigner, L. Lutterotti, M. Quirós, N.R. Serebryanaya, P. Moeck, R.T. Downs, A. Le Bail, Crystallography Open Database (COD): an open-access collection of crystal structures and platform for world-wide collaboration, Nucleic Acids Res. 40 (2012) D420–D427. https://doi.org/10.1093/nar/gkr900.

Graphical Abstract (for review)

Click here to access/download;Graphical Abstract (for review);fig-00-TOC.png

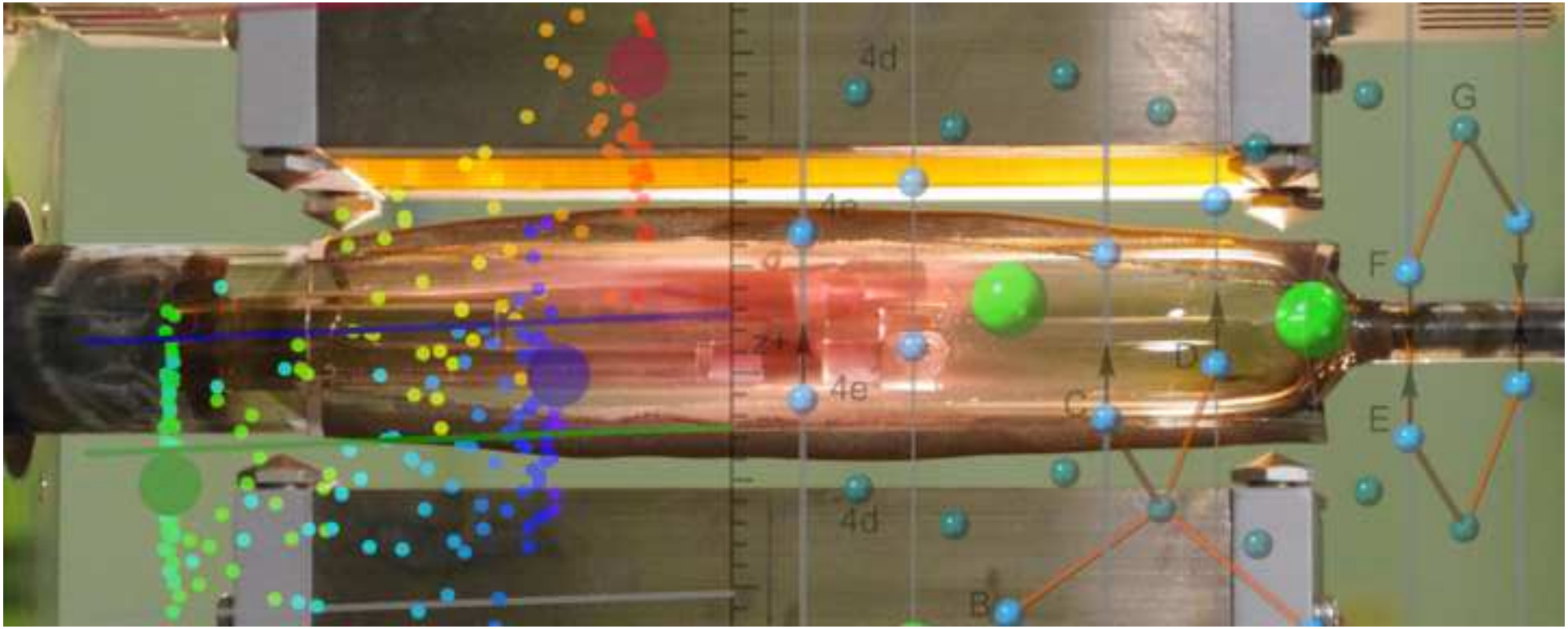

Figure 1

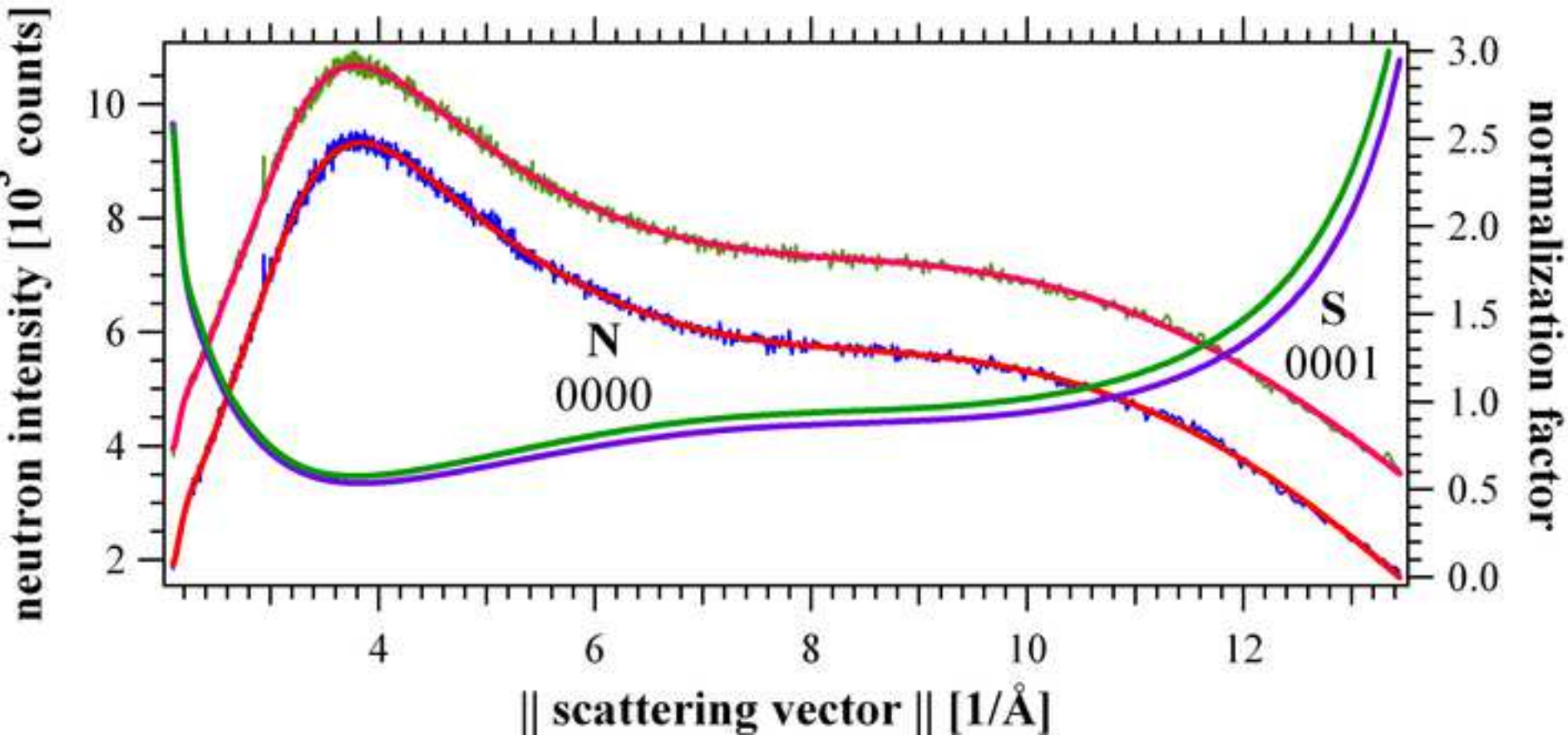

Figure 2

Click here to access/download;Figure;fig-02-Qplot1_labelled.png

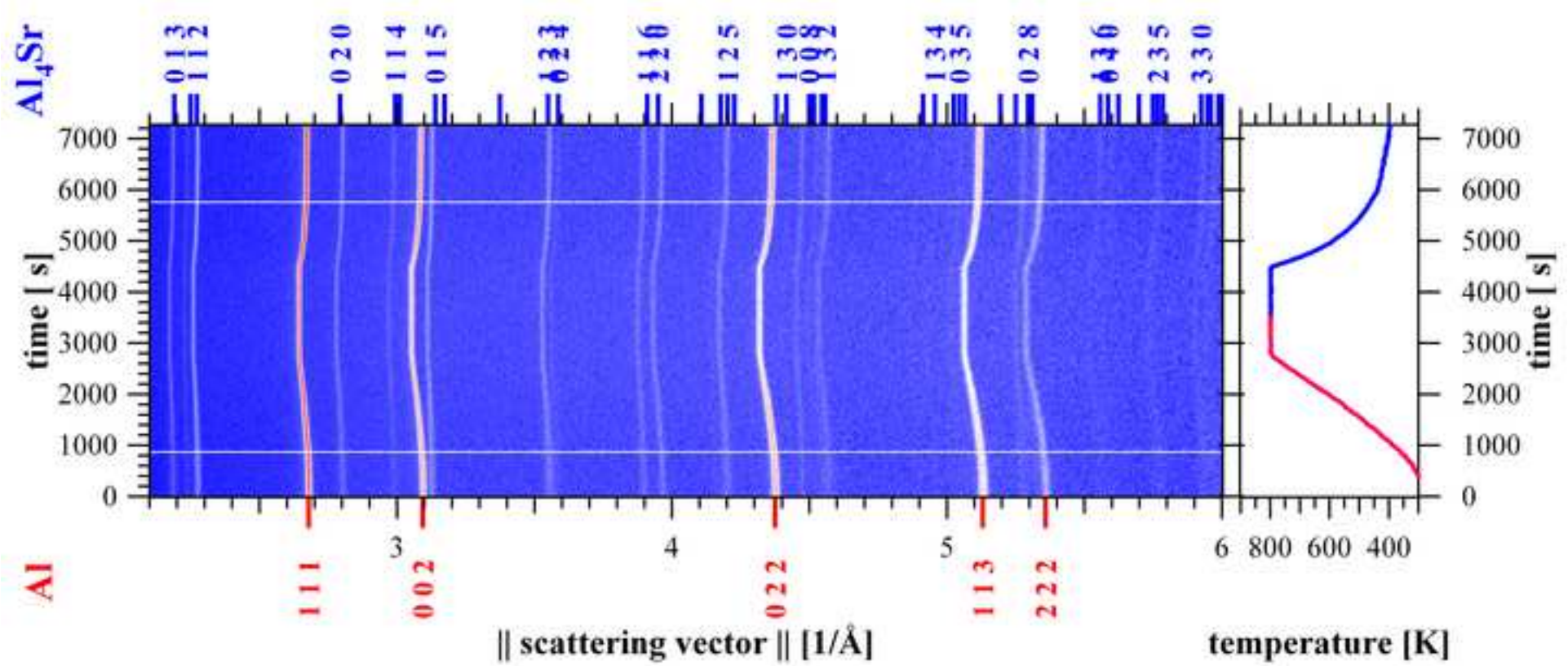

Figure 3

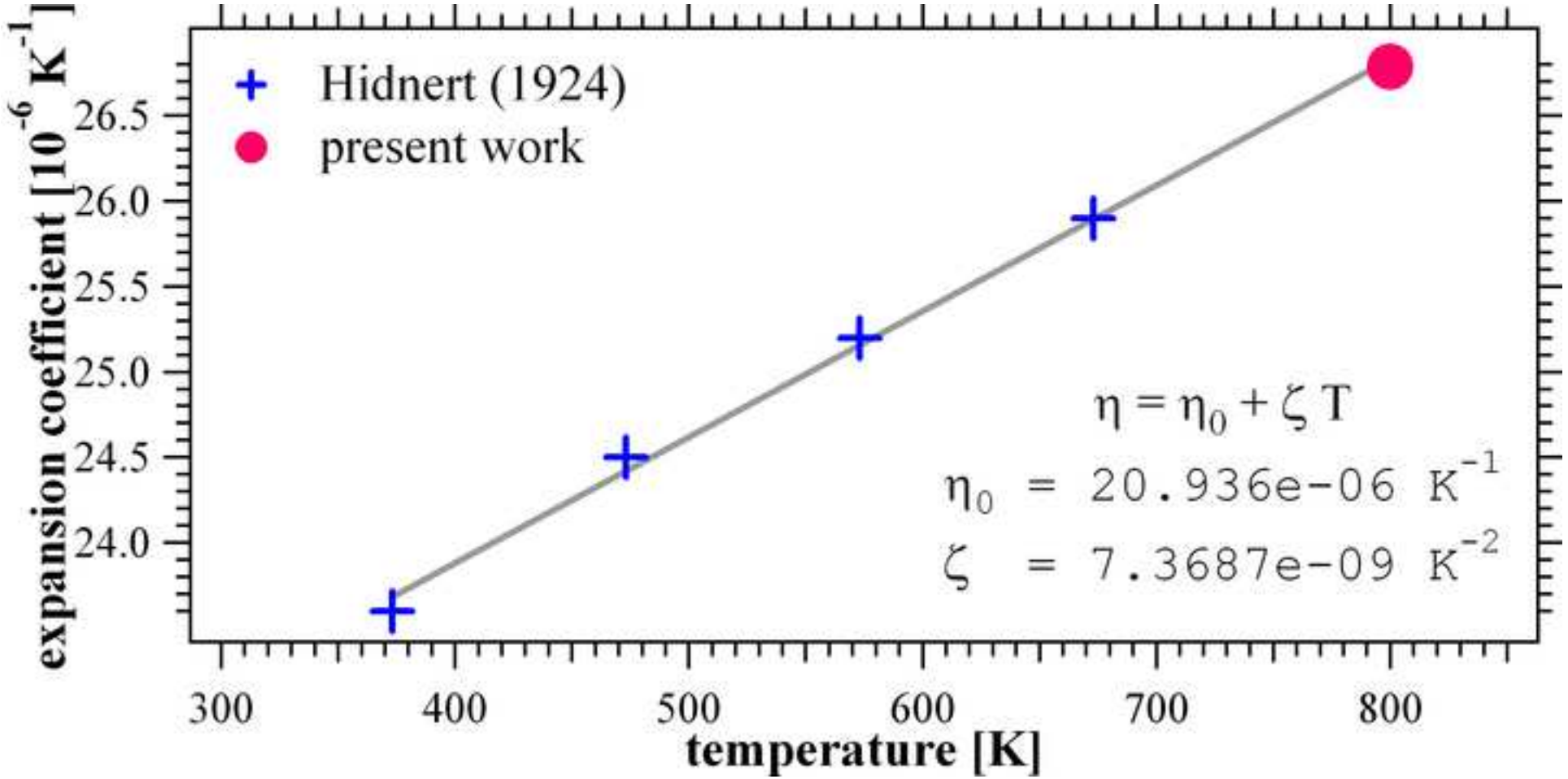

Figure 4

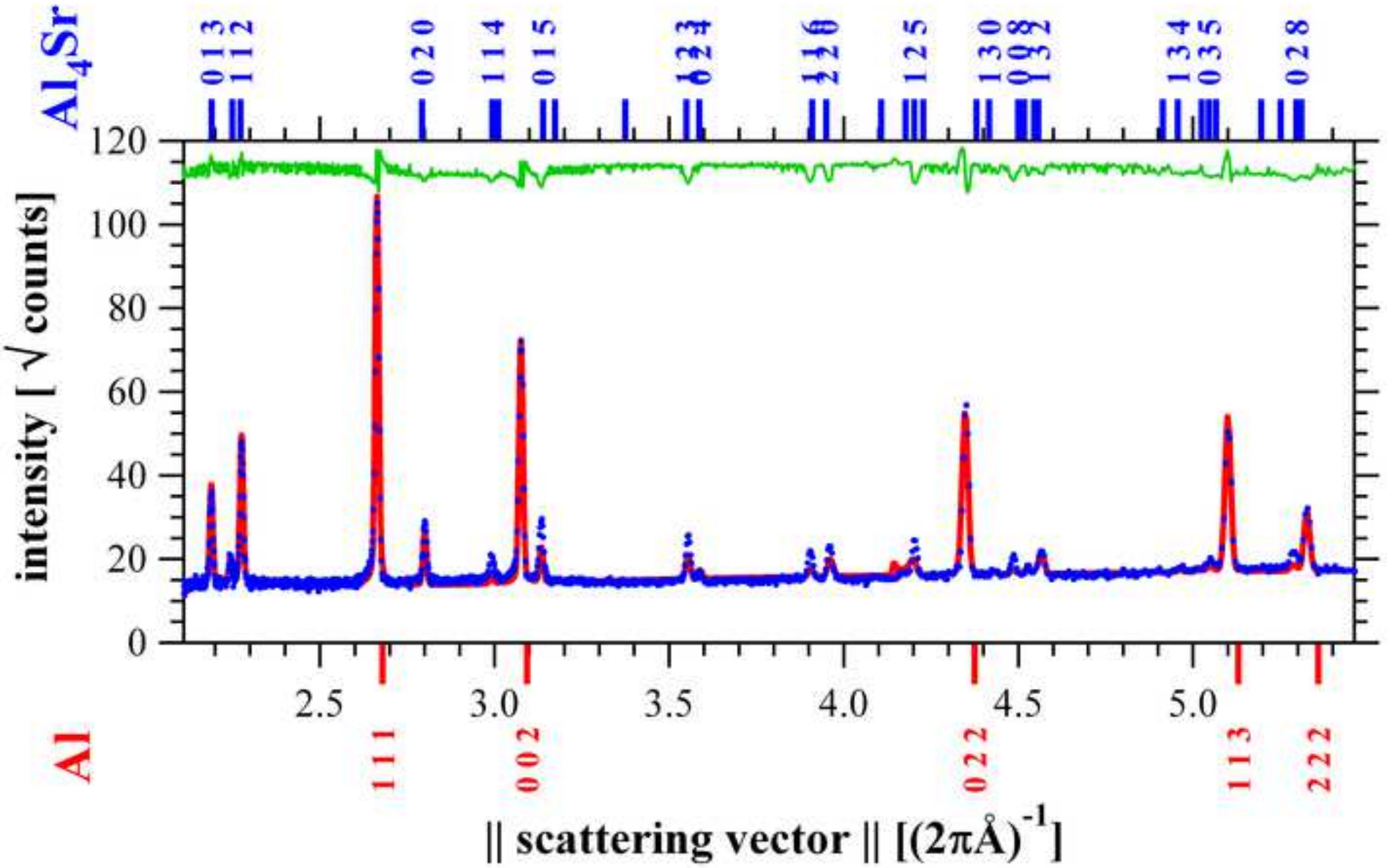

Figure 5

Click here to access/download;Figure;fig-05-Al4Sr1-tetrahedrons+hexagons-a.tif

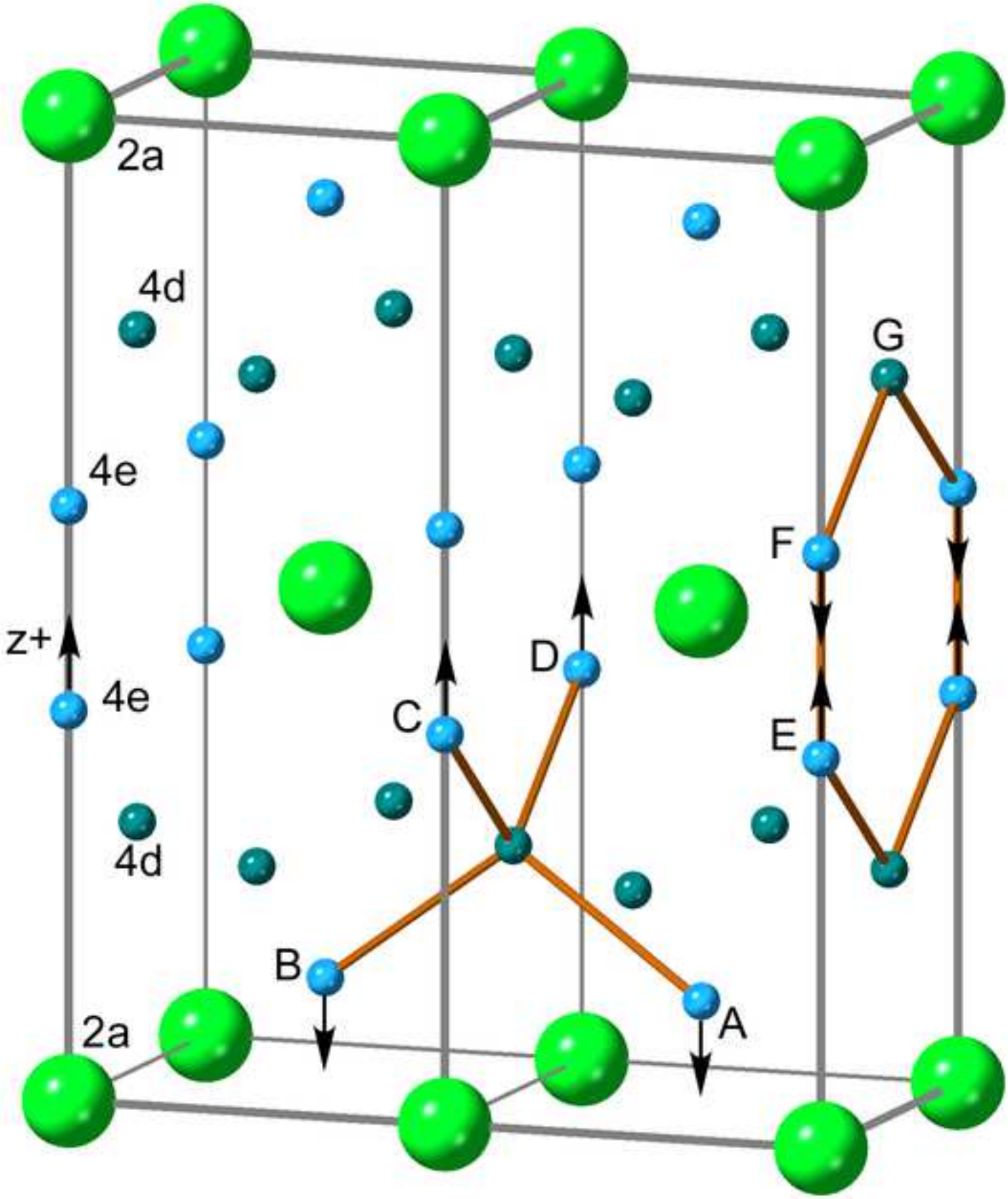

Figure 6b

Click here to access/download;Figure;fig-06b-Al-Scherrer_zoom_combo.png

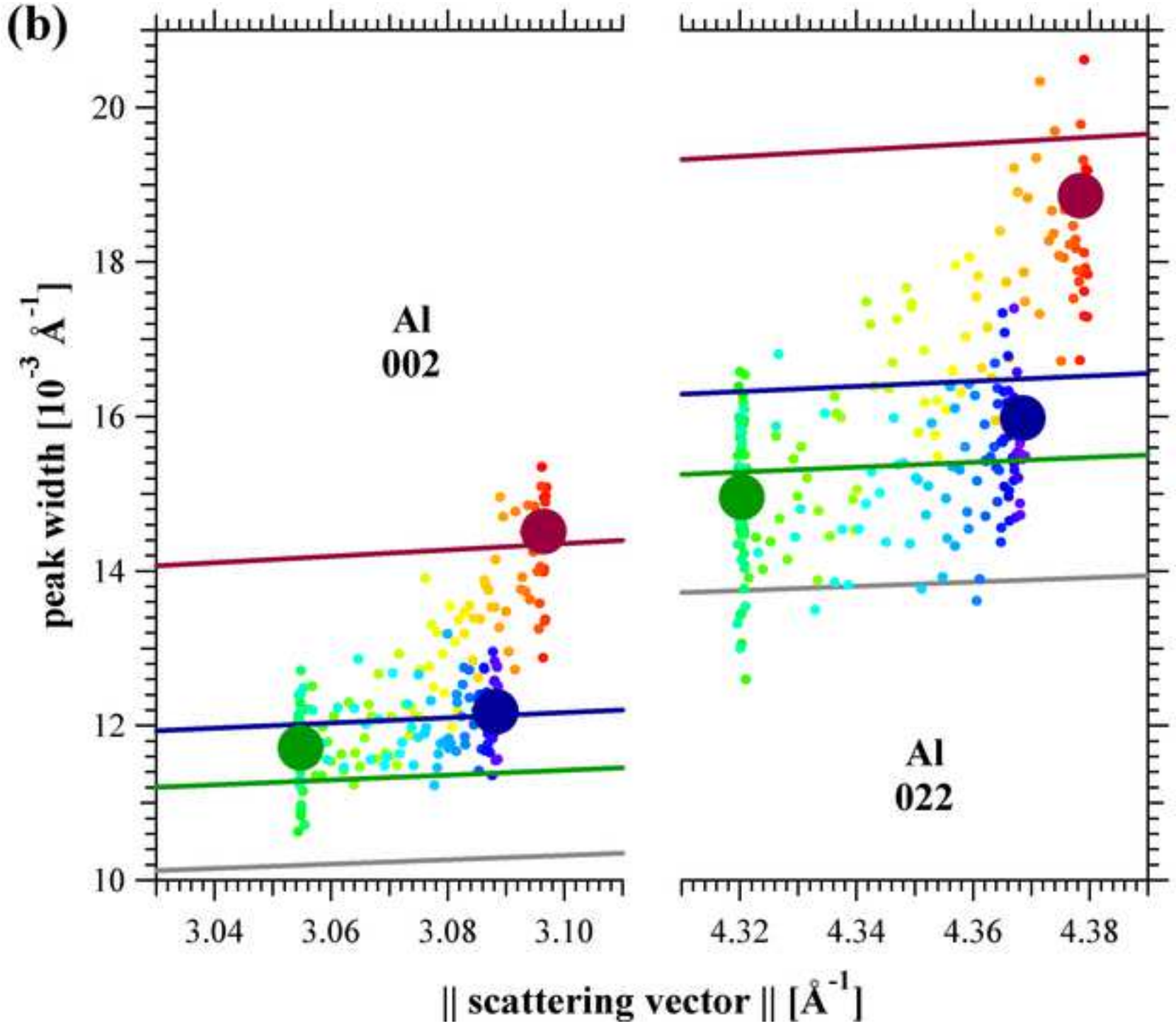

Figure 7

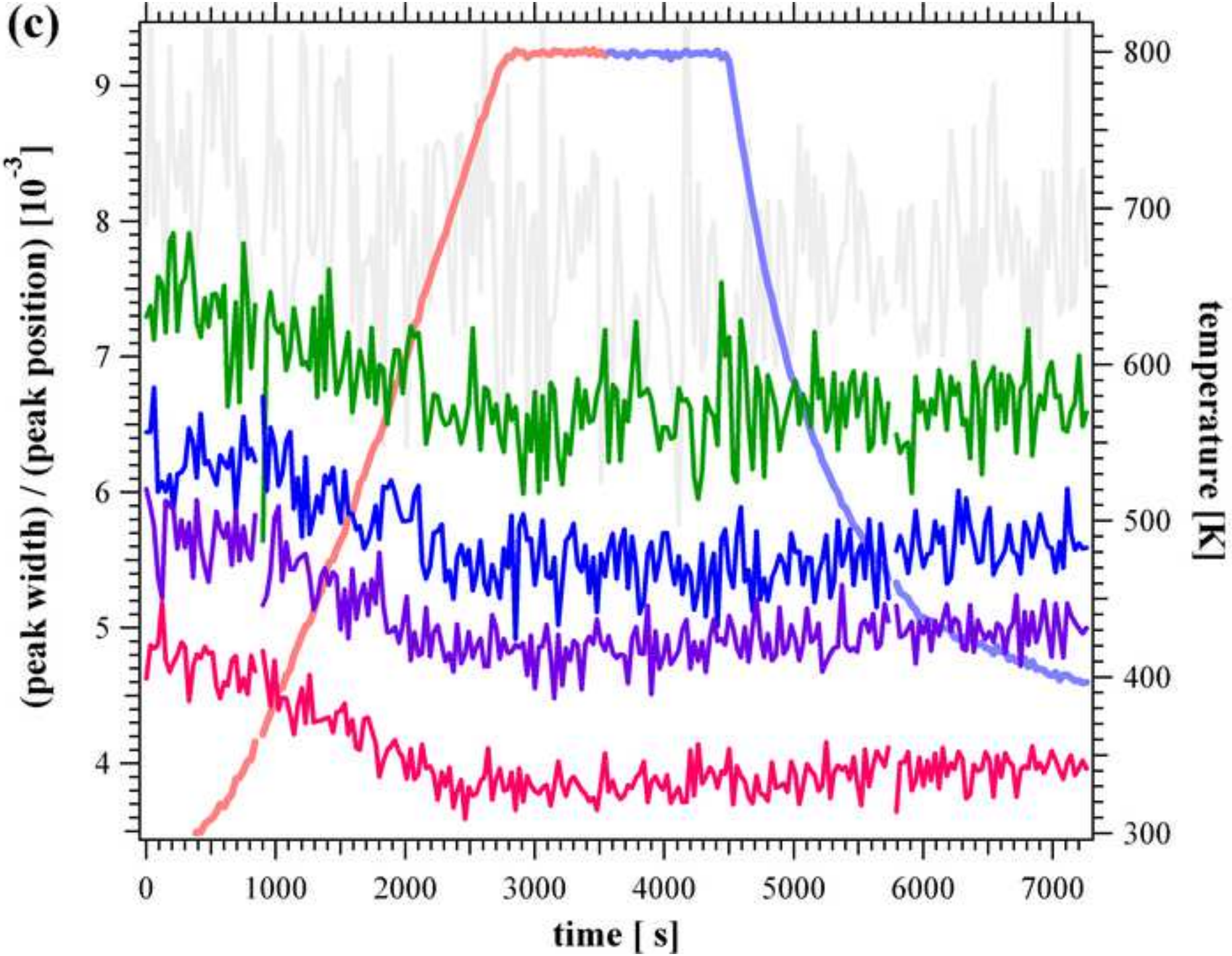

Figure 8

Click here to access/download;Figure;fig-08-ExpansionPlots.png

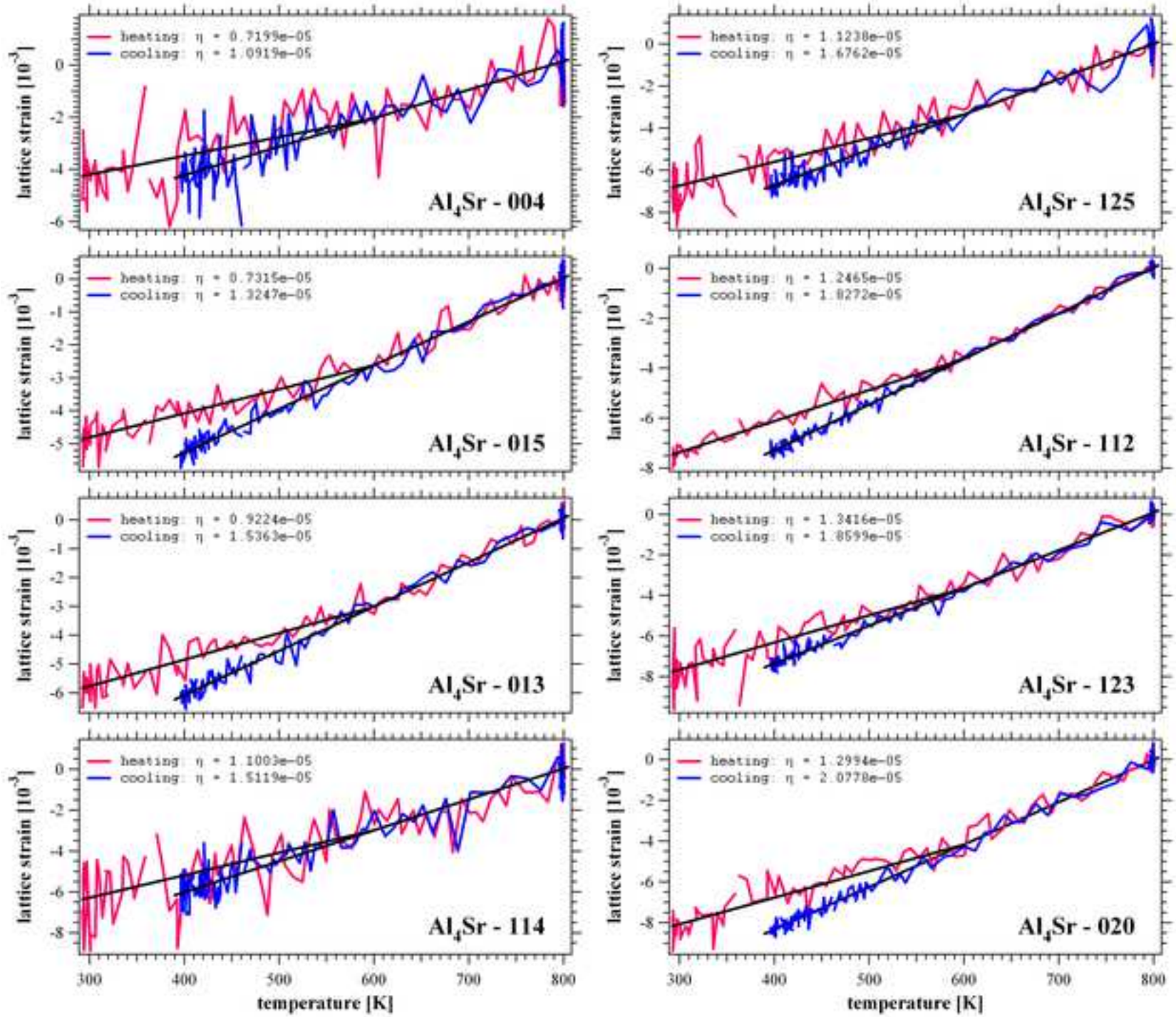

Figure 9a

Click here to access/download;Figure;fig-09a-Sin2Psi_h.png

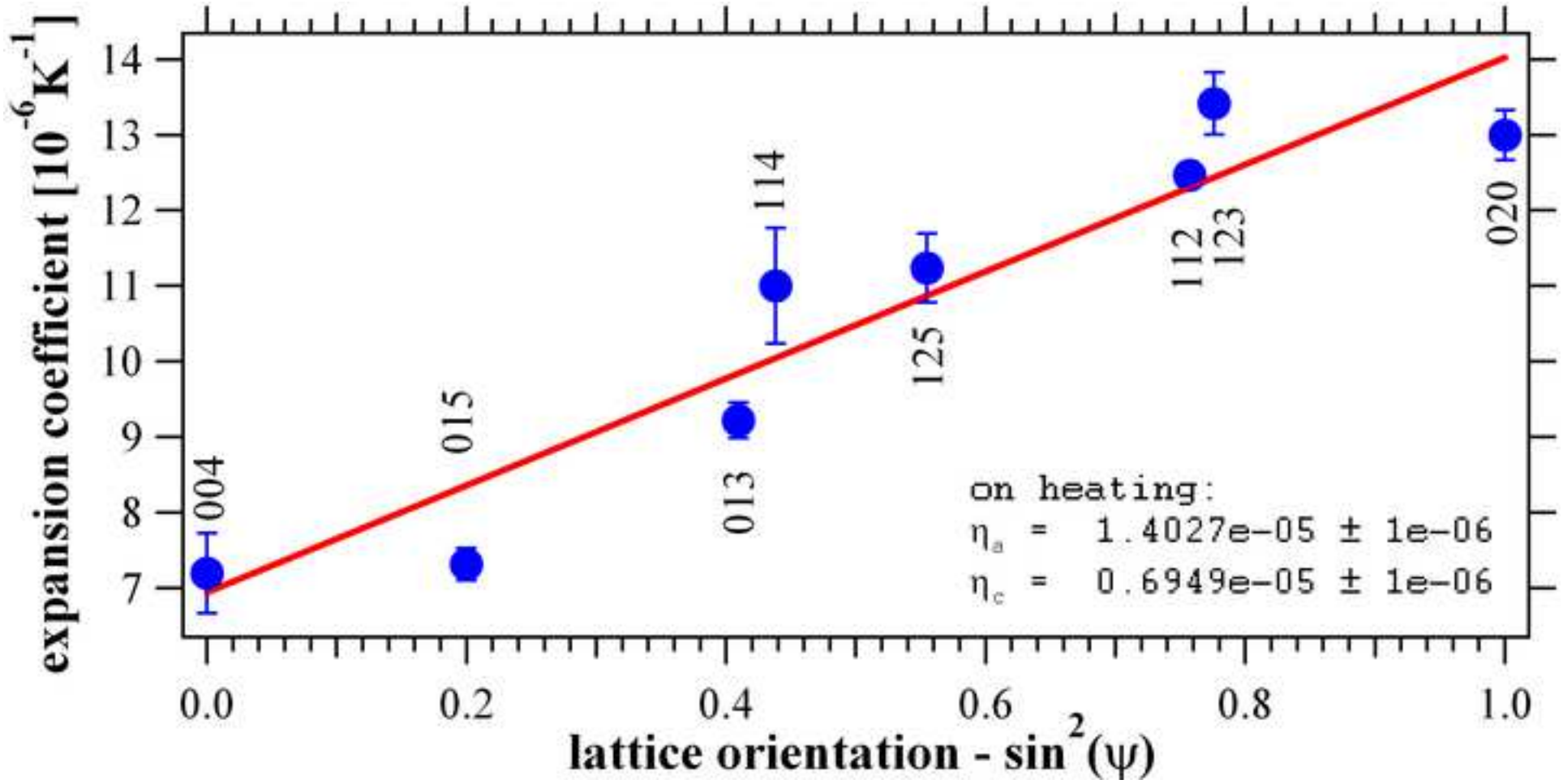

Figure 9b

Click here to access/download;Figure;fig-09b-Sin2Psi_c.png

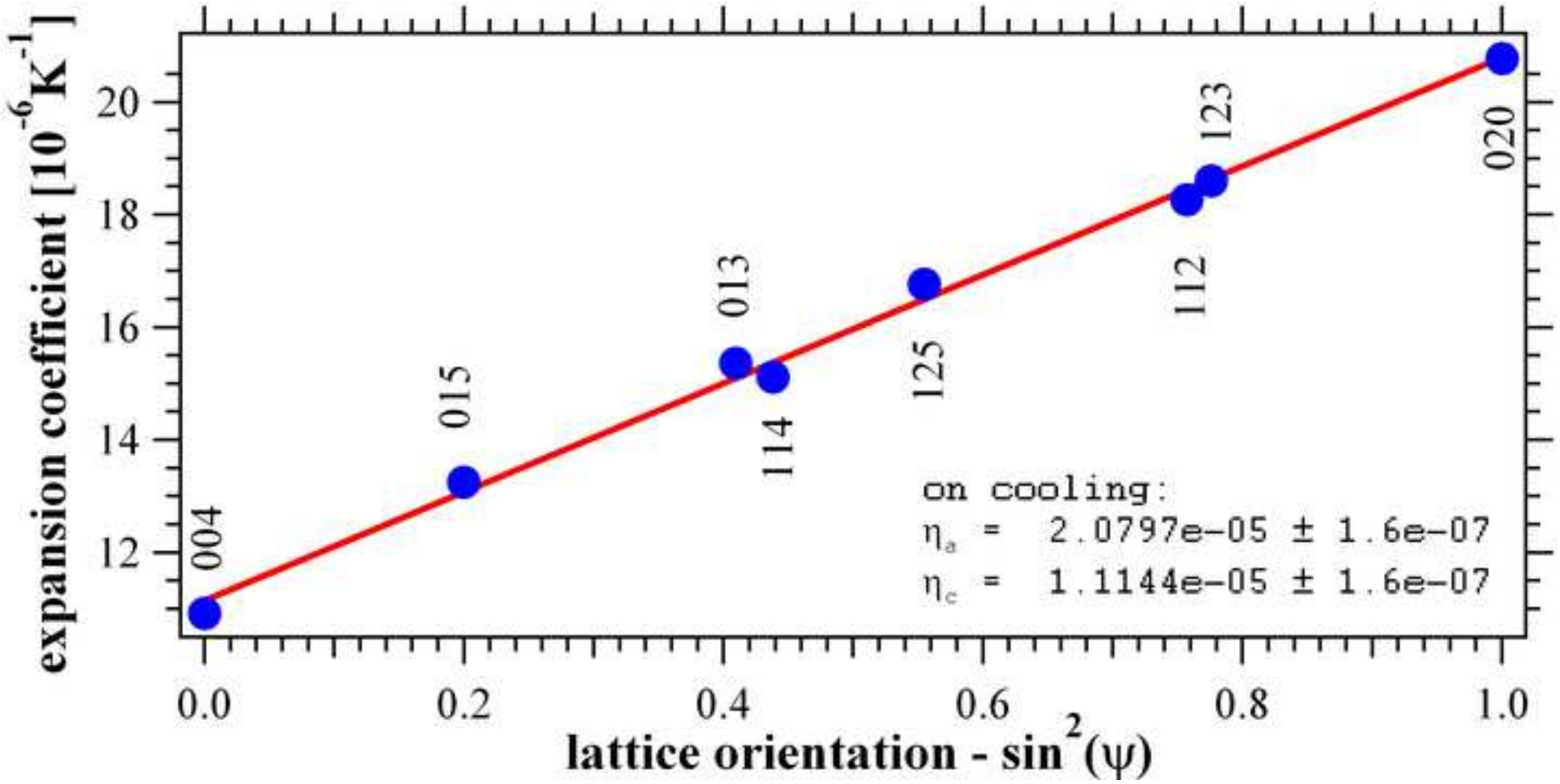

Figure 6a - revised

Click here to access/download;Figure;fig-06a-Al-Scherrer-new.png